


ARTICLE

Open Access

# Multifunctional electrochromic energy storage devices by chemical cross-linking: impact of a $\text{WO}_3\cdot\text{H}_2\text{O}$ nanoparticle-embedded chitosan thin film on amorphous $\text{WO}_3$ films

Bon-Ryul Koo<sup>1</sup>, Myeong-Hun Jo<sup>2</sup>, Kue-Ho Kim<sup>2</sup> and Hyo-Jin Ahn<sup>1,2</sup> 

## Abstract

With the advent of multifunctional devices with electrochromic (EC) behavior and electrochemical energy storage, complementary design of film structures using inorganic–organic materials has shown great potential for developing EC energy storage devices. Herein, hybrid films consisting of  $\text{WO}_3\cdot\text{H}_2\text{O}$  nanoparticle (WHNP)-embedded chitosan thin films on amorphous  $\text{WO}_3$  (a- $\text{WO}_3$ ) films were designed. By exploiting the hybrid effect of chitosan and WHNPs to generate unique chemical cross-linking between them, the designed films exhibited attractive EC behaviors compared to bare a- $\text{WO}_3$  films. These included fast switching speeds (4.0 s for coloration and 0.8 s for bleaching) due to enhanced electrical conductivity and Li-ion diffusivity, high coloration efficiency (62.4  $\text{cm}^2/\text{C}$ ) as a result of increased electrochemical activity, and superb long-cycling retention (91.5%) after 1000 cycles due to improved electrochemical stability. In addition, hybrid films exhibited a noticeable energy storage performance with a high specific capacitance (154.0 F/g at a current density of 2 A/g) and a stable rate capability as a result of improved electrochemical activity and fast electrical conductivity, respectively. This resulted in brighter illumination intensity for the 1.5-V white-light-emitting diode due to improved energy density compared to a bare a- $\text{WO}_3$  film. Therefore, the results suggest a new design strategy for materials to realize the coincident application of multifunctional devices with EC energy storage performance.

## Introduction

Presently, due to the growing energy demand with the increase in the world's population, many researchers are investigating innovative technologies to accelerate energy savings or energy efficiency to improve quality of life<sup>1–3</sup>. The use of electrochromic (EC) devices in the production of smart windows is imperative as a primary technology because they can facilitate energy savings by actively adjusting the sunlight flux that enters a building. The

ability to regulate heat flow into a building by changing the transparency or reflectance of an EC structure via an applied voltage results in a savings of >40% of the energy consumption<sup>4,5</sup>. In addition, EC devices are promising for use in a variety of optoelectronic applications, such as electronic displays, electronic paper, and rear-view mirrors, due to the realization of multiple colors by the adjustment of the operating voltage<sup>6</sup>. Recently, the implementation of electrochemical energy storage in EC devices has received significant interest as a potential avenue for expanding their applications. When the device performs optical modulation, a pseudocapacitance is usually generated via a reversible redox reaction at the electrode surface that results in the storage of charge<sup>7</sup>. Such a device can realize multiple functions of optical

Correspondence: Hyo-Jin Ahn ([hjahn@seoultech.ac.kr](mailto:hjahn@seoultech.ac.kr))

<sup>1</sup>Program of Materials Science & Engineering, Convergence Institute of Biomedical Engineering and Biomaterials, Seoul National University of Science and Technology, Seoul 01811, Korea

<sup>2</sup>Department of Materials Science and Engineering, Seoul National University of Science and Technology, Seoul 01811, Korea

© The Author(s) 2020



**Open Access** This article is licensed under a Creative Commons Attribution 4.0 International License, which permits use, sharing, adaptation, distribution and reproduction in any medium or format, as long as you give appropriate credit to the original author(s) and the source, provide a link to the Creative Commons license, and indicate if changes were made. The images or other third party material in this article are included in the article's Creative Commons license, unless indicated otherwise in a credit line to the material. If material is not included in the article's Creative Commons license and your intended use is not permitted by statutory regulation or exceeds the permitted use, you will need to obtain permission directly from the copyright holder. To view a copy of this license, visit <http://creativecommons.org/licenses/by/4.0/>.

modulation and energy storage/release simultaneously, and thus can automatically monitor the level of stored energy via variation of the optical properties (transmittance or color). The EC energy storage performance (optical modulation, coloration efficiency (CE), switching speed, long-cycling stability, specific capacitance, and rate capability) of multifunctional devices is believed to be attributed to the electrochemical double-behavior of electrons and cations on active materials. In this case, the optical modulation, CE, and specific capacitance are mainly related to the degree of insertion/extraction of electrons and cations into/from the active materials in response to the applied voltage and the degree of the switching speed, and the rate capability is directly determined by the ion diffusivity and electron conductivity on active materials<sup>8,9</sup>. Among the active materials of multifunctional devices classified as inorganic materials (transition metal oxides, Prussian blue-based materials, etc.) and organic materials (conjugated polymers, arylamine-based polymers, viologens, etc.), tungsten oxide ( $\text{WO}_3$ ) is an advanced pseudocapacitive material with favorable EC characteristics of reversible color variation from optical transparency to deep blue, in addition to high contrast, good electrochemical stability, and low cost<sup>10</sup>. Typically, the  $\text{WO}_3$  materials exhibit a significant difference in their electrochemical behavior related to the EC performance of their amorphous and crystalline structures. For crystalline  $\text{WO}_3$ , there are limitations associated with ion movement because their densely packed structure and electroactive site near larger grains cause a reduction in electrochemical performance while ensuring electrochemical cycling stability<sup>11</sup>. On the other hand, amorphous  $\text{WO}_3$  (a- $\text{WO}_3$ ) facilitates a favorable movement of ions due to the organization of a loosely packed atomic structure with large tunnels, leading to superb electrochemical kinetics compared to the crystalline  $\text{WO}_3$  structure<sup>12</sup>. However, to the best of our knowledge, a- $\text{WO}_3$ -based devices unfortunately encounter limitations of the EC energy storage performance, such as the CE value (20–38  $\text{cm}^2/\text{C}$ ), switching speed (3.0–5.0 min for  $1524 \times 3048 \text{ mm}^2$  of SageGlass®), and specific capacitance (60–100 F/g) as a result of a low diffusion coefficient and a long diffusion pathway for ion insertion, which still remains an important factor to be addressed for the realization of high-performance multifunctional devices<sup>13,14</sup>.

In various efforts to improve the EC energy storage performance using a- $\text{WO}_3$  films, the design of the film structure by tuning the crystal structure and morphology of a- $\text{WO}_3$  materials and the introduction of complexation with polymer materials have been performed by some researchers<sup>15–17</sup>. There was a recent attempt to produce complementary heterostructure  $\text{WO}_3$  films with crystalline  $\text{WO}_3$  nanoparticles in an a- $\text{WO}_3$  matrix that can produce more electroactive sites and accelerated ion

kinetics, which improves the transmittance modulation of the EC devices, together with a high diffusion coefficient and charge/discharge density to increase the electrochemical performance for energy storage<sup>18</sup>. As another effective route, the complexation of a- $\text{WO}_3$  with polymer materials (polyaniline and polypyrrole) has received much attention with regard to improving the EC energy storage performance of next-generation active materials. Although, these composite film structures mostly exhibit good switching speeds below 5.0 s due to the superb electrical conductivity of polymer-based materials, they still suffer from serious degradation of the electrochemical activity and kinetics under successive operating conditions, as a result of physically mixed inorganic/organic film structures to limit charge transport by boundary scattering between two different materials and to aggravate adhesion with substrates by ununiform distribution of inorganic particles in an organic matrix. This contributes to the critical point for the effective development of multifunctional devices with EC energy storage performance<sup>19–22</sup>. Therefore, the novel design of hybrid a- $\text{WO}_3$  film structures based on the unique advantages of each inorganic and organic material is suggested as an important approach for the improvement of EC energy storage performance. This has not been considered in previous reports on multifunctional devices with both EC behavior and electrochemical energy storage.

These findings encourage us to concentrate on utilizing chitosan as an innovative organic material for improving EC energy storage performance. Chitosan, which is produced by the deacetylation of chitin in processing the discarded remnants of shrimp, is one of the most abundant and renewable natural polymers, with biocompatible and biodegradable characteristics, and thus has been widely used in the molecular separation and water treatment<sup>23,24</sup>. In addition, chitosan, as a functional polymer with abundant hydroxyl and amine groups, has the potential to be utilized as an N-doping source on carbon materials to achieve good photocatalytic performance and as an effective membrane, as a result of cross-linking of the chitosan to achieve superb pervaporation performance to separate various aqueous organic sols<sup>24,25</sup>. However, since there is limited electrochemical performance when chitosan is used autonomously as an electroactive material owing to its intrinsic molecular structure, which is electrochemically inactive, in this study, we should consider a complementary design with chitosan thin films as a unique medium for accelerating the electrochemical behavior of the a- $\text{WO}_3$  films to enhance EC energy storage performance.

Herein, we designed novel hybrid films of chitosan embedded with  $\text{WO}_3 \cdot \text{H}_2\text{O}$  nanoparticles (WHNPs) on a- $\text{WO}_3$  films to implement fast and stable EC energy storage performance of multifunctional devices. Interestingly,

chitosan is not only used as an intensive accelerator for electrochemical behavior with cations due to its abundant functional groups but is also utilized as a linking medium to connect other elements via protonated amine groups ( $-\text{NH}_3^+$ ) under acidic conditions. This phenomenon is expected to facilitate a remarkable chemical linking to the WHNPs with oxygen vacancies and cross-linking between the chitosan molecules and thus provides improved electrochemical kinetics, as well as stability of the  $\alpha\text{-WO}_3$ -based films. Based on this unique phenomenon, we also demonstrate how the EC energy storage performance is affected by the hybrid effect of the chitosan and the WHNPs on the  $\alpha\text{-WO}_3$ -based films.

### Materials and methods

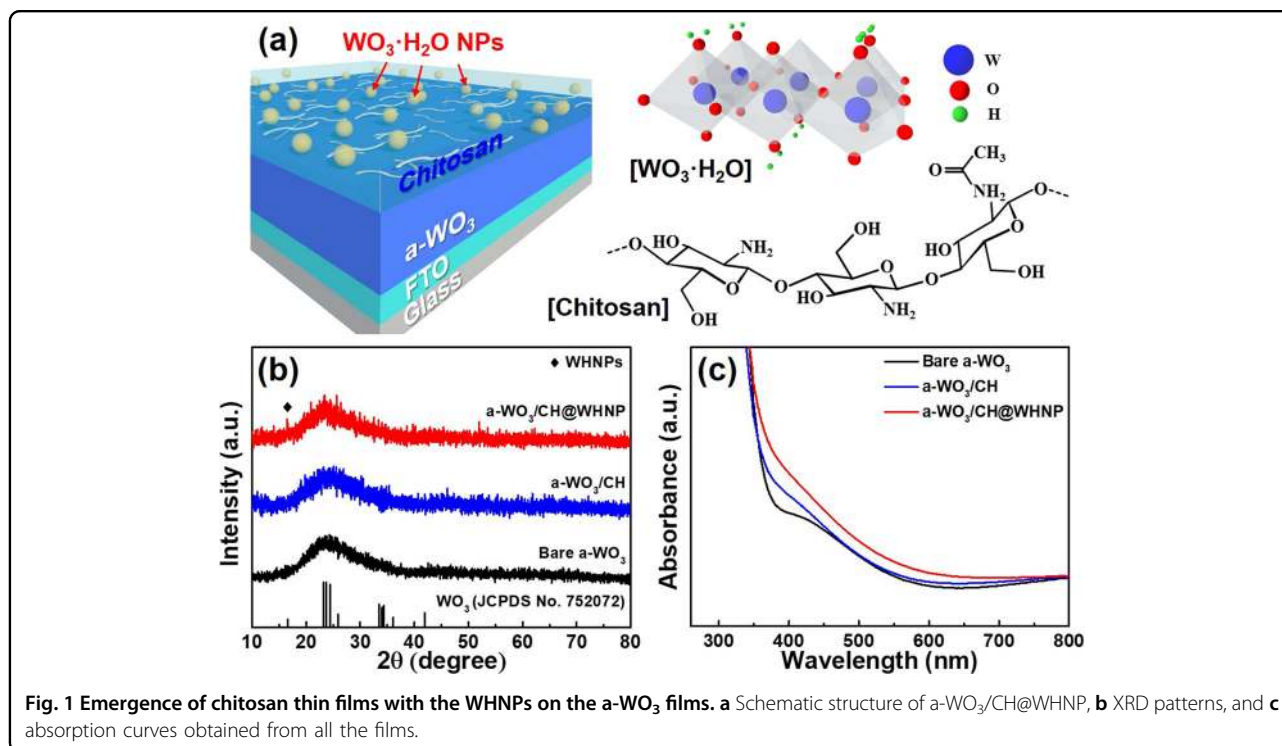
$\alpha\text{-WO}_3$ /WHNP-embedded chitosan hybrid films were prepared by using the spin-coating method. First, the preparation of the  $\alpha\text{-WO}_3$  films was achieved by spin-coating a sol-solution of 10 wt% tungsten(VI) chloride ( $\text{WCl}_6$ , Aldrich) dissolved in 2-propanol ( $(\text{CH}_3)_2\text{CHOH}$ , Aldrich) on commercial F-doped  $\text{SnO}_2$  (FTO) films ( Pilkington,  $8.0 \Omega/\square$ ), followed by annealing at  $300^\circ\text{C}$  in air for 1 h (herein named bare  $\alpha\text{-WO}_3$ ). The WHNPs for embedding in the chitosan thin films were fabricated using the hydrothermal method. In summary, 0.05 M tungstic acid ( $\text{H}_2\text{WO}_4$ , Aldrich) and 6 M hydrochloric acid (HCl, Samchun) were dissolved in deionized (DI) water. Then, the prepared solution was transferred into a Teflon-lined autoclave and maintained at  $180^\circ\text{C}$  for 1 h in an oven. Afterward, the autoclave was cooled, and the resultant precipitate was washed with DI water to obtain pure WHNPs. Subsequently, the obtained WHNPs (0.01 wt%) were mixed with the chitosan solution prepared by dissolving 0.5 wt% chitosan (medium molecular weight, Aldrich) in DI water with 1 vol% acetic acid ( $\text{CH}_3\text{CO}_2\text{H}$ , Aldrich) and then spin-coating the mixture onto the  $\alpha\text{-WO}_3$  films at a speed of 2,000 rpm for 30 s, resulting in the formation of  $\alpha\text{-WO}_3$ /WHNP-embedded chitosan hybrid films (referred to as  $\alpha\text{-WO}_3$ /CH@WHNP) after drying at  $80^\circ\text{C}$  for 1 h. For comparison,  $\alpha\text{-WO}_3$  films with only chitosan were fabricated (referred to as  $\alpha\text{-WO}_3$ /CH).

The investigation of crystal structure was performed by using X-ray diffraction (XRD, Rigaku D/Max-2500 diffractometer using  $\text{Cu } K_\alpha$  radiation). The chemical binding state was characterized via X-ray photoelectron spectroscopy (XPS, AXIS ultra-delay line detector equipped with an  $\text{Al } K_\alpha$  X-ray source, KBSI Daedeok Headquarters) and Fourier transform infrared (FTIR) spectroscopy (Thermo Fisher Scientific, Nicolet iS50). The surface and cross-section morphologies were revealed via field-emission scanning electron microscopy (FESEM, Hitachi S-4800) and atomic force microscopy (AFM, diDimensionTM 3100). The element distribution was analyzed using an

energy dispersive spectrometer (EDS), and the electrical and optical properties were studied using a Hall-effect measurement system (Ecopia, HMS-3000) and ultraviolet–visible (UV–vis) spectroscopy (Perkin–Elmer, Lambda–35), respectively. The electrochemical analysis was conducted using a potentiostat/galvanostat (PGSTAT302N, FRA32M, Metrohm Autolab B.V., the Netherlands) and electrochemical impedance spectroscopy (EIS) in a three electrode system with a 1 M  $\text{LiClO}_4$  electrolyte (in propylene carbonate (PC)), a platinum (Pt) wire as the counter electrode, and a silver (Ag) wire as the reference electrode. The wettability of the electrolyte at the interface of all films was characterized using a contact angle meter (CAM 200, Ksv Instruments). The EC energy storage performance of a single electrode and multi-functional device was measured in situ by a combination of a potentiostat/galvanostat and UV–vis spectroscopy.

### Results and discussion

As a unique approach to the enhancement of the EC energy storage performance of  $\alpha\text{-WO}_3$  films, we introduced a WHNP-embedded chitosan thin film onto their surface, as shown in Fig. 1a. Although chitosan lacks EC behavior due to the absence of a phase transition with the applied potential, its large number of  $-\text{NH}_2$  and  $-\text{OH}$  functional groups can act as accelerators for electrochemical behavior with cations<sup>26,27</sup>. In addition, this hybrid material can exhibit a strong chelate effect on the elements of the WHNPs due to the special functional group of the chitosan that has a complementary impact on the electrochemical behavior<sup>28</sup>. To confirm the elaborate structure of bare  $\alpha\text{-WO}_3$ ,  $\alpha\text{-WO}_3$ /CH, and  $\alpha\text{-WO}_3$ /CH@WHNP, XRD analysis was conducted on all the films prepared on glass substrates. As shown in Fig. 1b, bare  $\alpha\text{-WO}_3$  gives rise to a broad diffraction peak centered at  $\sim 23.1^\circ$ , which is indicative of the presence of the  $\alpha\text{-WO}_3$  structure<sup>29</sup>. With the introduction of the chitosan thin film on  $\alpha\text{-WO}_3$  films ( $\alpha\text{-WO}_3$ /CH), there is a slight decrease in the diffraction intensity without structural variation of the  $\alpha\text{-WO}_3$ . For  $\alpha\text{-WO}_3$ /CH@WHNP, the presence of an additional sharp diffraction peak at  $16.5^\circ$  was observed, which is well matched to the (020) plane of  $\text{WO}_3\cdot\text{H}_2\text{O}$  with an orthorhombic structure, as shown in the enlarged XRD results (Supplementary Fig. 1) for the WHNPs (Supplementary Fig. 2). The introduction of chitosan and WHNPs is also confirmed by a comparison of the absorption spectra measured from all the films. Compared to the spectra of bare  $\alpha\text{-WO}_3$ , the spectra of  $\alpha\text{-WO}_3$ /CH reveal an absorption band at  $\sim 400.0 \text{ nm}$  due to functional groups along the chains of chitosan<sup>29,30</sup>. In addition, for  $\alpha\text{-WO}_3$ /CH@WHNP, there is an absorption band in the visible region due to the existence of the WHNPs on the  $\text{WO}_3$  film (see Fig. 1c)<sup>6</sup>. Thus, these results indicate the successful introduction of chitosan

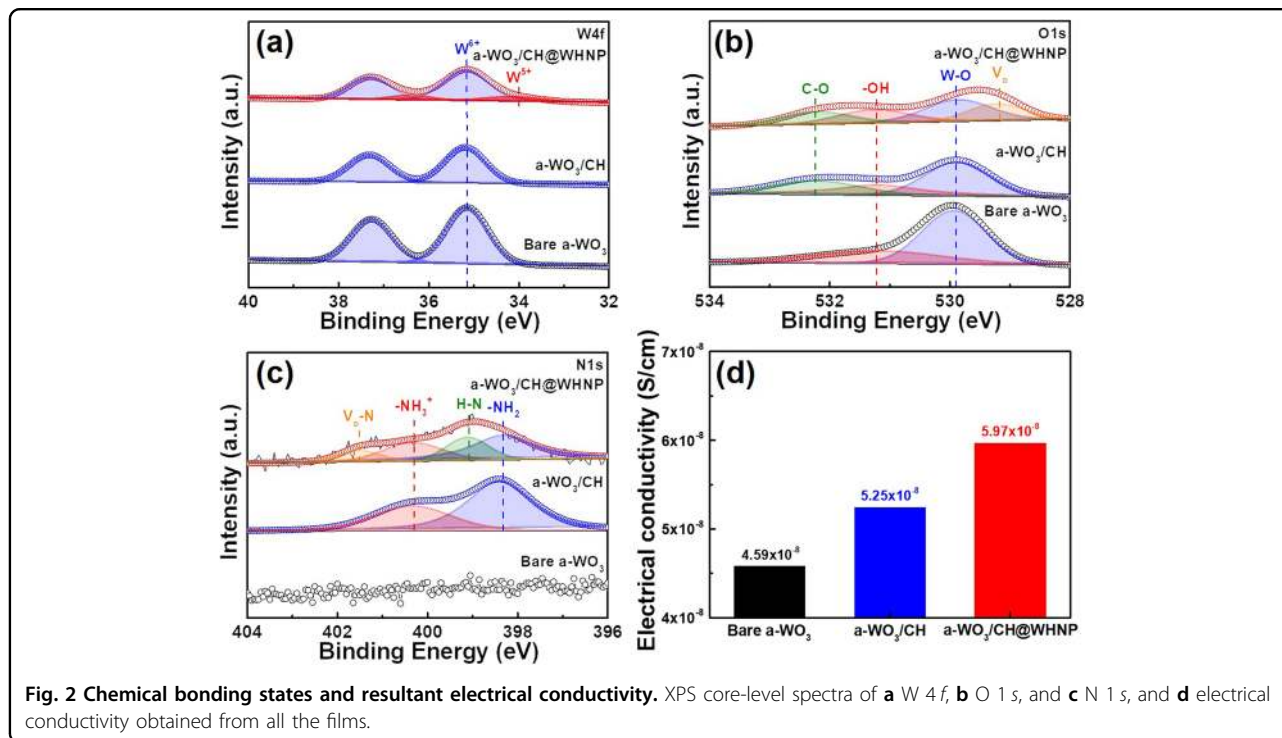


thin films with WHNPs on a-WO<sub>3</sub> films using a spin-coating method.

To evaluate the chemical characteristics of the films due to the hybrid effect of the chitosan and the WHNPs, XPS analysis was performed, and the results are shown in Fig. 2a–c. All binding energies of the XPS spectra were fixed by referencing the C 1s peak at 284.5 eV. In the W 4f XPS core-level spectra shown in Fig. 2a, the dominant peak of all films was observed at ~35.1 eV for W 4f<sub>7/2</sub> and ~37.2 eV for W 4f<sub>5/2</sub>. This is attributed to the binding energy of W<sup>6+</sup> in the a-WO<sub>3</sub> phases<sup>32</sup>. For a-WO<sub>3</sub>/CH@WHNP, there is an additional pair of doublets at ~34.3 eV for W 4f<sub>7/2</sub> and ~36.5 eV for W 4f<sub>5/2</sub> that corresponds to W<sup>5+</sup>, based on the evidence of 2.3% oxygen vacancies (V<sub>o</sub>) of nonstoichiometric WHNPs<sup>33</sup>. From Fig. 2b, a definite distinction of the O 1s XPS core-level spectra among the films is observed. Compared to bare a-WO<sub>3</sub>, which exhibits two characteristic peaks at ~529.9 and ~531.2 eV due to the W–O and –OH bonds, respectively, there is an additional characteristic peak at ~532.2 eV due to the C–O bond in a-WO<sub>3</sub>/CH<sup>29</sup>. In addition, the –OH/W–O peak area ratio of a-WO<sub>3</sub>/CH (56.4%) was higher than that of bare a-WO<sub>3</sub> (46.8%). These results are attributed to the chitosan thin film with carbonyl groups that interact with hydroxyl groups, as reported by V. D. Pickenhahn et al. and M. G. Dekamin et al.<sup>34,35</sup>. a-WO<sub>3</sub>/CH is responsible for the characteristic peaks at ~398.3 and ~400.3 eV in the N 1s XPS core-level spectra that are assigned to the amine group (–NH<sub>2</sub>) and

protonated amine group (–NH<sub>3</sub><sup>+</sup>) of chitosan, respectively (Fig. 2c). These groups can be useful for electron transport in the films and result in the improvement of the electrical conductivity (5.25 × 10<sup>–8</sup> S/cm) compared to bare a-WO<sub>3</sub> (4.59 × 10<sup>–8</sup> S/cm), as confirmed in Fig. 2d<sup>36,37</sup>. In addition, –NH<sub>3</sub><sup>+</sup> that is easily formed from –NH<sub>2</sub> of chitosan under acidic conditions can lead to the formation of mechanically strong chitosan thin films that are cross-linked due to electrostatic interactions between them<sup>38</sup>. The O 1s XPS core-level spectra of a-WO<sub>3</sub>/CH@WHNP have a characteristic peak related to V<sub>o</sub> of the WHNPs at 529.2 eV that is well-matched to the presence of W<sup>5+</sup>, as shown in the W 4f XPS core-level spectra. In addition, the existence of V<sub>o</sub> can also be explained by optical bandgap narrowing of a-WO<sub>3</sub>/CH@WHNP caused by extra carriers by the WHNP compared to that of a-WO<sub>3</sub>/CH (Supplementary Fig. 3)<sup>39,40</sup>. This can serve as the color or energy storage center and is attributed to excess electrons and the pathway for the improvement of electrical conductivity<sup>41</sup>. However, despite the unique features of the WHNPs, in the previous report, there is a limitation with respect to achieving satisfactory electrical conductivity for electrochemical behavior because of the increasing interparticle boundary due to the minute size of the WHNPs in the films<sup>42</sup>. Surprisingly, for a-WO<sub>3</sub>/CH@WHNP, two characteristic peaks that are distinct from that of a-WO<sub>3</sub>/CH are emitted at 399.0 and 401.5 eV in the N 1s XPS core-level spectra (Fig. 2c). These peaks can be attributed to the H–N





and  $V_o$ -N bonds. According to Shao and Choi et al., the characteristic peaks are related to anionic N- to form O-Ti-N or O-W-N linkages by bonding with positively charged elements<sup>43–46</sup>. Therefore, we believe that the H (in the edge region) and  $V_o$  of the WHNPs with partially positive charges can form chemical bonds with the amine-related groups of chitosan due to its chelation effect. This is confirmed by the N 1s XPS core-level spectra of the films that were fabricated with pure  $WO_3$  nanoparticles ( $a-WO_3/CH@WO_3$  NP), as confirmed by the emission of  $W^{6+}$  peaks in Supplementary Fig. 4a, which show the absence of the H-N and  $V_o$ -N bonds (Supplementary Fig. 4b). This result is also confirmed by the FTIR results that show strong H-N stretching vibrations at 3230 per cm on  $a-WO_3/CH@WHNP$ , while weakening the  $NH_2$  and  $NH_3^+$  stretching vibrations related to the functional groups of chitosan (Supplementary Fig. 5). Therefore, the chemical interaction of the chitosan thin films that act as a conducting matrix and the WHNPs with oxygen vacancies can become the dominant route for improving electron transport. Thus, there is an improvement in the electrical conductivity of the hybrid films ( $a-WO_3/CH@WHNP$ ) compared to the other films.

Figure 3a–c shows top-view FESEM images of bare  $a-WO_3$ ,  $a-WO_3/CH$ , and  $a-WO_3/CH@WHNP$ . In the case of bare  $a-WO_3$  (Fig. 3a), a densely uniform structure without any discernible particulates is observed throughout the surface of the films<sup>8</sup>. In the case of  $a-WO_3/CH$ , as shown in Fig. 3b, although the surface structure appears to be similar to that of bare  $a-WO_3$ , the

highest root mean square roughness ( $R_{ms}$ ) obtained from the AFM analysis (Supplementary Fig. 6b) is lower than that of bare  $a-WO_3$  (Supplementary Fig. 6a). This implies that chitosan thin films are introduced in the range of  $\sim 16.0$ – $25.0$  nm, as shown in Supplementary Fig. 7a. In Fig. 3c,  $a-WO_3/CH@WHNP$  has well-dispersed NPs on the films with diameters in the range of  $\sim 6.2$ – $11.9$  nm (Supplementary Fig. 7b). This may be attributable to the static repulsion caused by the electrostatic interaction between  $-NH_3^+$  of the chitosan and the surface of the WHNPs<sup>31</sup>. Interestingly, there is no noticeable variation in the  $R_{ms}$  of  $a-WO_3/CH@WHNP$  (Supplementary Fig. 6c) compared to that of  $a-WO_3/CH$  despite the existence of the WHNPs. This indicates that the WHNPs are uniformly embedded in the chitosan thin films without any changes in their surface structure, which is expected to clearly demonstrate the hybrid effects on the EC energy storage performance using chitosan and the WHNPs. As additional proof to confirm the presence of chitosan and the WHNPs, the EDS results of the WHNP-embedded chitosan thin films prepared on glass substrates (Fig. 3d) show the elemental distribution of N from chitosan and W from the WHNPs. Therefore, in accordance with the XRD, XPS, SEM, and AFM results discussed above, the elaborate architecture of the hybrid films ( $a-WO_3/CH@WHNP$ ) is clearly confirmed.

To provide further evidence of the effects of the WHNP-embedded chitosan thin films on the  $a-WO_3$  films, the interfacial resistance of the films was measured using EIS. Figure 4a shows the Nyquist plots for three

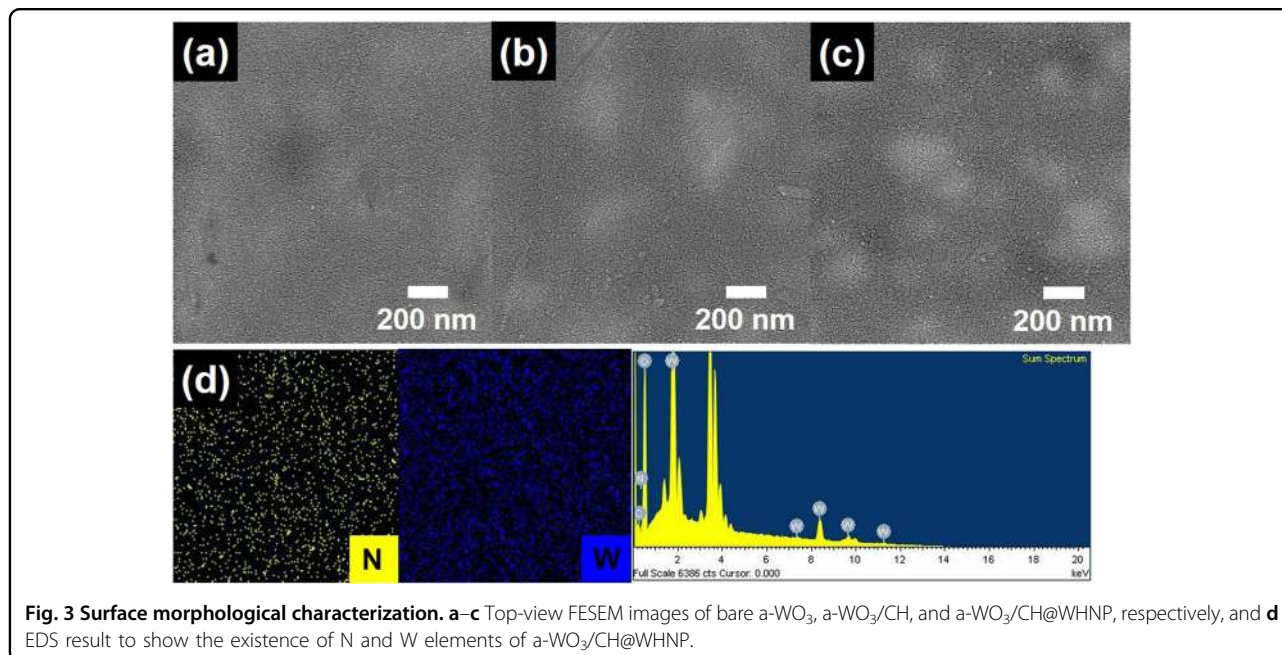
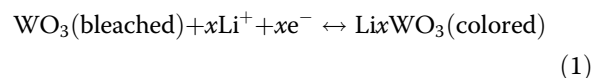


**Fig. 3** Surface morphological characterization. **a–c** Top-view FESEM images of bare a-WO<sub>3</sub>, a-WO<sub>3</sub>/CH, and a-WO<sub>3</sub>/CH@WHNP, respectively, and **d** EDS result to show the existence of N and W elements of a-WO<sub>3</sub>/CH@WHNP.

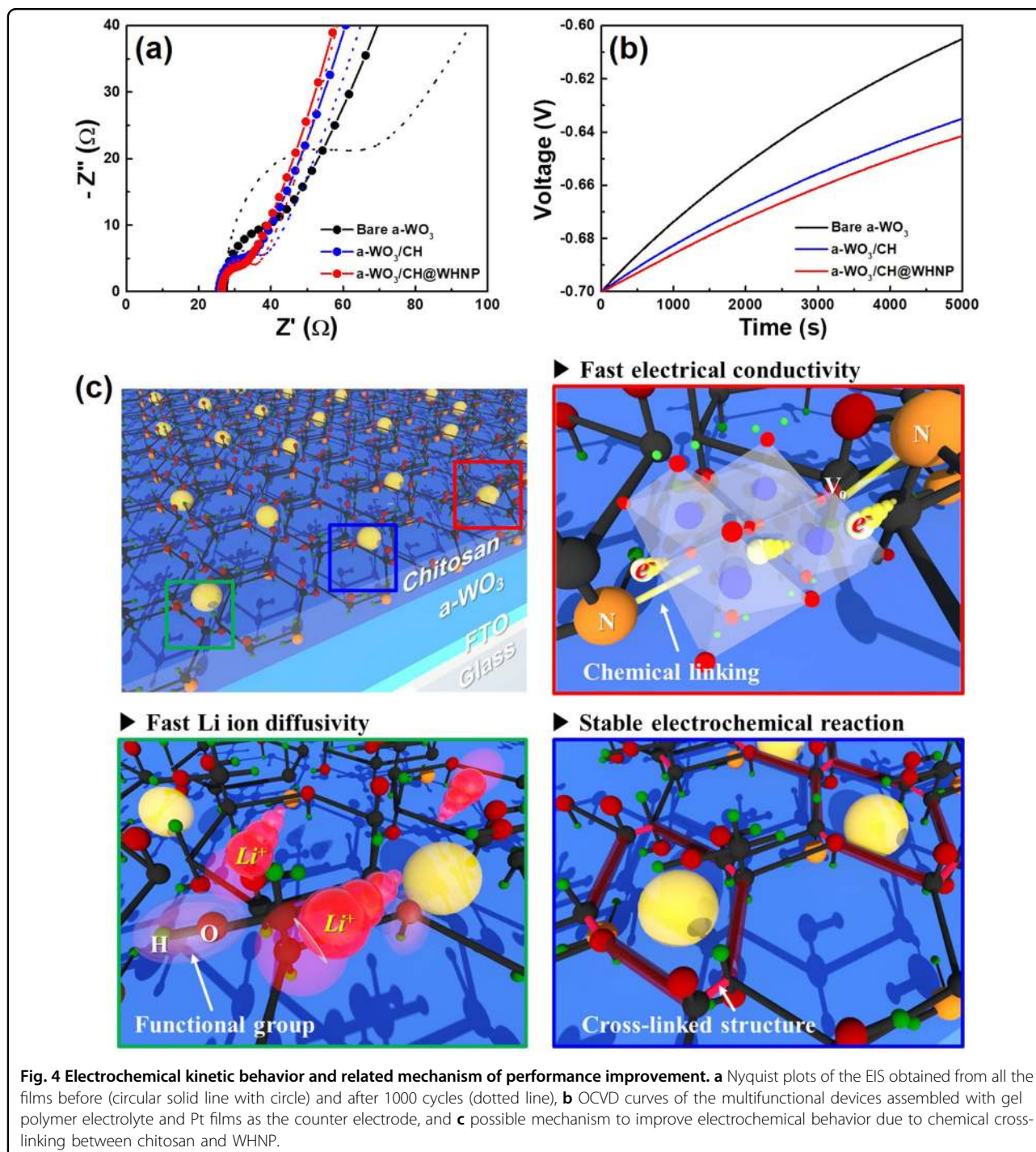
characteristic zones related to the sheet resistance of the FTO films (series resistance,  $R_s$ ), the charge transfer resistance from the active material in contact with the electrolyte (radius of the semicircle arc,  $R_{ct}$ ), and the electrolyte ion diffusion impedance (Warburg region,  $Z_w$ ). These results are summarized in Supplementary Table 1 by fitting the EIS results<sup>47</sup>. As expected, although there is no variation in the series resistance among the films because of the identical sheet resistance of the FTO films, the smaller semicircle and shorter Warburg region of a-WO<sub>3</sub>/CH@WHNP compared to the others is noted, which are indicative of enhanced electrical conductivity and Li-ion diffusivity, respectively, due to the introduction of the WHNP-embedded chitosan thin films. This result indicates that the existence of chitosan thin films can cause EC stability by decreasing the charge transfer resistance of the a-WO<sub>3</sub> films as a result of electrochemical behavior in which charges are freely obtained from a-WO<sub>3</sub> films. In addition, the improvement in the kinetic characteristics was also confirmed by the open-circuit voltage decay (OCVD) curves obtained from multifunctional devices with all film active materials and Pt films as the counter electrodes by the removal of the coloring potential (−0.7 V; Fig. 4b). Given that the OCVD of the devices is associated with the leakage current generated due to interfacial resistance between the components, the relaxed OCVD of a-WO<sub>3</sub>/CH@WHNP compared to those of the other films can indicate the ability to facilitate efficient transport of the electrons and Li ions, without undergoing losses at the active material<sup>48,49</sup>. These striking kinetic characteristics are attributable to the unique impact of chemical linking between the chitosan and the WHNPs (Fig. 4c). More interestingly,

there is no critical variation in the semicircle and the Warburg region on the electrodes with the chitosan thin films (a-WO<sub>3</sub>/CH and a-WO<sub>3</sub>/CH@WHNP) after 1000 cycles of electrochemical processes, compared to bare a-WO<sub>3</sub>, which exhibits a larger semicircle and longer Warburg region (1000 cycles), as summarized in Supplementary Table 1. This result highlights additional advantages of chitosan thin films that improve the electrochemical stability of the active materials during repetitive EC processes due to strongly cross-linked structures via electrostatic interactions between chitosan molecules (Fig. 4c).

The electrochemical performance of all films in terms of application in multifunctional devices was evaluated using the CV curve measured in the three electrode system. By analyzing the resulting curve in the potential region from −0.7 to 1.0 V (vs. Ag wire) at a scan rate of 20 mV/s (Fig. 5a), it is observed that all the films have a broad redox curve without any sharp peaks. This is indicative of the EC behavior of a-WO<sub>3</sub> to reversibly vary the color from deep blue in the colored state to transparent in the bleached state and vice versa, by double insertion/extraction of electrons and Li ions into/out of the films, as indicated by the following equation (Eq. (1))<sup>50</sup>:



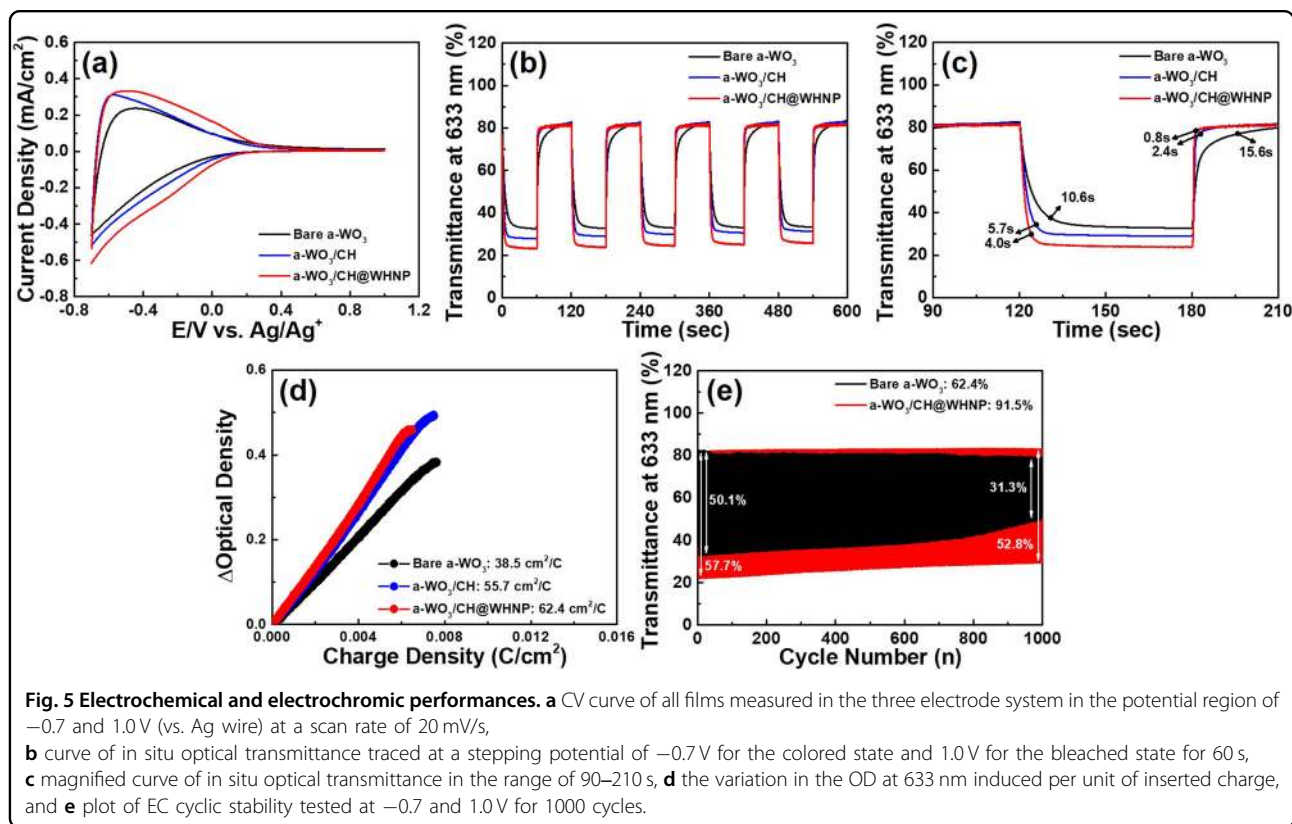
It is also noted that the CV curve of a-WO<sub>3</sub>/CH@WHNP has a larger area in proportion to the redox current density than those of bare a-WO<sub>3</sub> and a-WO<sub>3</sub>/CH, indicating superb electrochemical activity. This is mainly attributed to the presence of the WHNP-embedded



chitosan on the a-WO<sub>3</sub> films. By comparing bare a-WO<sub>3</sub> and a-WO<sub>3</sub>/CH, it is observed that the introduction of chitosan thin films improves the electrochemical activity, which may be due to the increase in surface wettability with respect to the electrolyte to facilitate the access of the electrolyte to the surface of the electrodes where the electrochemical reaction occurs, given that the functional groups of chitosan, such as the hydroxyl and amine

groups, cause the film's surface to be strongly hydrophilic. This was confirmed by the decreased contact angle of the electrolyte at the interface (Supplementary Fig. 8)<sup>51–54</sup>. Moreover, the hybrid WHNPs in chitosan thin films can induce enhanced insertion/extraction of Li ions because the intercalated water molecules in the WO<sub>3</sub>·H<sub>2</sub>O have a wider interplanar spacing ( $d = 5.36 \text{ \AA}$ ) than those of WO<sub>3</sub> ( $d = 3.84 \text{ \AA}$ ), thereby suggesting





outstanding electrochemical activity to facilitate good reaction capacity of electrons and Li ions in the films<sup>55,56</sup>. In Supplementary Fig. 9, the correlation between the increase in the peak current density ( $J_p$ ) and the square root of the scan rate ( $C_o$ ) in the CV curve provides information about the Li-ion diffusion coefficient ( $D$ ) from the electrolyte to the film's surface<sup>6</sup>. As determined according to the Randles–Sevcik equation, a faster Li-ion diffusion coefficient of a-WO<sub>3</sub>/CH@WHNP ( $10.49 \times 10^{-9}$  cm<sup>2</sup>/s) compared to the others ( $2.95 \times 10^{-9}$  cm<sup>2</sup>/s for bare a-WO<sub>3</sub> and  $7.69 \times 10^{-9}$  cm<sup>2</sup>/s for a-WO<sub>3</sub>/CH) is observed. This is due to the improved electrical conductivity caused by chemical linking between chitosan and the WHNPs in the hybrid films (Fig. 2d). This electrochemical behavior can serve as an important factor in the improvement in EC energy storage performance<sup>11,32</sup>. In the in situ optical transmittance curve that was traced by scanning the applied potential of  $-0.7$  V for the colored state and  $1.0$  V for the bleached state for  $60$  s (Fig. 5b), the critical aspects of transmittance modulation ( $\Delta T$ ) and switching speed can be confirmed. As summarized in Table 1, the transmittance modulation ( $\Delta T = \text{transmittance value at the bleached state } (T_b) - \text{transmittance value at the colored state } (T_c)$ ) of a-WO<sub>3</sub>/CH@WHNP is up to  $57.7\%$ , which is higher than the value of  $7.6\%$  for bare a-WO<sub>3</sub> due to the increased electrochemical activity of the hybrid effect

with chitosan and the WHNPs, which is also proved by the transmittance spectra in the wavelength range of  $400$ – $800$  nm traced at different working states (Supplementary Fig. 10). The switching speed, which is defined as the coloration/bleaching time extracted for a  $90\%$  transmittance modulation at  $633.0$  nm, was much faster in a-WO<sub>3</sub>/CH@WHNP (Fig. 5c). Improvements in the values by  $19.5$  times for the bleached state and  $2.6$  times for the colored state were observed when compared to that of bare a-WO<sub>3</sub>. These results are excellent relative to those obtained from previous studies of WO<sub>3</sub>-based EC films, as shown in Supplementary Table 2. The striking enhancement is primarily due to the increased electrical conductivity and Li-ion diffusivity via strong chemical interaction between chitosan and the WHNPs. Another important factor that must be considered to comprehensively evaluate the performance of EC devices is the CE, defined as the variation in the optical density (OD) induced per unit of inserted charge ( $Q/A$ ), which can be obtained from Eqs. (2)–(3):<sup>55</sup>

$$CE = \Delta OD / (Q/A) \quad (2)$$

$$\Delta OD = \log(T_b/T_c) \quad (3)$$

The obtained CE value from the curve of Fig. 5d is  $62.4$  cm<sup>2</sup>/C for a-WO<sub>3</sub>/CH@WHNP, which is increased by  $162.0\%$  compared to that of bare a-WO<sub>3</sub>. This is



**Table 1** Summary of EC performance parameters of all films.

Samples	$T_b$ (%)	$T_c$ (%)	Transmittance modulation (%)	Coloration speed (s)	Bleaching speed (s)	CE ( $\text{cm}^2/\text{C}$ )
Bare a-WO <sub>3</sub>	82.7	32.6	50.1	10.6	15.6	38.5
a-WO <sub>3</sub> /CH	82.1	28.9	53.2	5.7	2.4	55.7
a-WO <sub>3</sub> /CH@WHNP	81.4	23.7	57.7	4.0	0.8	62.4

correlated with the synergistic effects of the wide transmittance modulation caused by the improved electrochemical activity and the efficient charge transport induced by the increased electrical conductivity and Li-ion diffusion coefficient. This is primarily due to the hybrid effect of chitosan and the WHNPs introduced on the a-WO<sub>3</sub> films, which is also confirmed by the performance comparison between a-WO<sub>3</sub>/CH@WHNP and a-WO<sub>3</sub> films with only WHNP (a-WO<sub>3</sub>@WHNP; Supplementary Fig. 11). The cycling retention can be a major concern in the practical application of EC devices, while the transmittance modulation of bare a-WO<sub>3</sub> rapidly degrades to 62.4% after 1000 cycles, whereas that of a-WO<sub>3</sub>/CH@WHNP is maintained at 91.5% of its original transmittance modulation (Fig. 5e). This superb cycling retention of the EC films can be generated by the cross-linked effect of the chitosan thin film to relax the structural variation of a-WO<sub>3</sub> and WHNPs, which can be confirmed by the stable electrochemical behavior shown in the EIS result measured after 1000 cycles (Fig. 4a and Supplementary Table 1).

The aforementioned EC behavior associated with the reversible redox reaction of Li ions and electrons, as represented in CV curves (Fig. 5a), can also achieve the appropriate capacitive performance as the origin of the energy storage<sup>48,49</sup>. The capacitive performance in terms of the specific capacitance ( $C_{\text{sp}}$ , F/g), the energy density ( $E$ , Wh/kg), and the power density ( $P$ , kW/kg) is obtained by using the following equations (Eqs. (4)–(6)):<sup>57,58</sup>

$$C_{\text{sp}} = 4I/(m dV/dt) \quad (4)$$

$$E = C_{\text{sp}} V^2/8 \quad (5)$$

$$P = E/dt \quad (6)$$

where  $I$  (A) is the current at charging and discharging states,  $m$  (g) is the mass loading of the active material (0.00031 g for bare a-WO<sub>3</sub> and 0.00042 g for a-WO<sub>3</sub>/CH@WHNP),  $dV$  is the voltage drop upon discharging, and  $dt$  (s) is the total discharging time. Figure 6a shows the galvanostatic charge/discharge curves of all the films for a current density of 2 A/g. There is a symmetry between the charging and discharging curves that indicate good reversibility of the films during charge/discharge processes. Compared to a-WO<sub>3</sub>, the discharge slope is not

as steep, and there is an extinction of the drop for a-WO<sub>3</sub>/CH@WHNP. This is induced by the enhanced electrical conductivity and Li-ion diffusion coefficient of the EC films, thus resulting in a higher capacity for energy savings<sup>59</sup>. As indicated by the specific capacitance calculated from the discharging curves (Fig. 6b), a-WO<sub>3</sub>/CH@WHNP reaches up to 154.0 F/g at a current density of 2 A/g, which is higher than that of bare a-WO<sub>3</sub> (95.0 F/g). With the increase in the current density to 10 A/g, although there is a rapid decrease in the specific capacitance on bare a-WO<sub>3</sub> (24.7% compared to that of 2 A/g), a-WO<sub>3</sub>/CH@WHNP maintains a specific capacitance of 94.6%, demonstrating good rate capability. This is due to accelerated electrochemical kinetics as a result of the hybrid effect with chitosan and WHNP. Furthermore, based on the Ragone plot showing energy density vs. power density (Fig. 6c), it is noted that the energy density of a-WO<sub>3</sub>/CH@WHNP reached 55.2 Wh/kg at 6.1 kW/kg and was 52.7 Wh/kg at 30.6 kW/kg. These values are much higher than those obtained for bare a-WO<sub>3</sub>. This is attributed to the improved electrochemical activity of a-WO<sub>3</sub>/CH@WHNP because the energy density and power density are determined by the voltage difference ( $\Delta V$ ) between active electrodes. To further evaluate the practical application of bare a-WO<sub>3</sub> and a-WO<sub>3</sub>/CH@WHNP as active materials for EC energy storage, we assembled solid-state cells with multiple functions of electrochromism and energy storage using a gel polymer electrolyte (PMMA + LiClO<sub>4</sub> + PC) and a NiO film as the counter electrode. As shown in Fig. 6d, the transmittance spectra of the cells have smaller values as the applied negative voltages are increased, resulting in a transmittance modulation of 46.0% for bare a-WO<sub>3</sub> and 50.6% for a-WO<sub>3</sub>/CH@WHNP at 633 nm, which is comparable to the performance of intrinsic a-WO<sub>3</sub>/CH@WHNP, despite the use of a polymer electrolyte. The contract variation of the cell accounts for the one-to-one relationship between the transmittance and the voltage, which can be an important criterion for the visual monitoring of the states of energy storage (discharging for the bleached state (Supplementary Fig. 12a) and charging for the colored state (Supplementary Fig. 12b))<sup>60,61</sup>. Interestingly, when the 1.5-V white light-emitting diode (LED, FK185, 1.5-V 6-LED LIGHT) is powered by the two solid-state cells, the illumination intensity of a-WO<sub>3</sub>/CH@WHNP (68.0 lux,

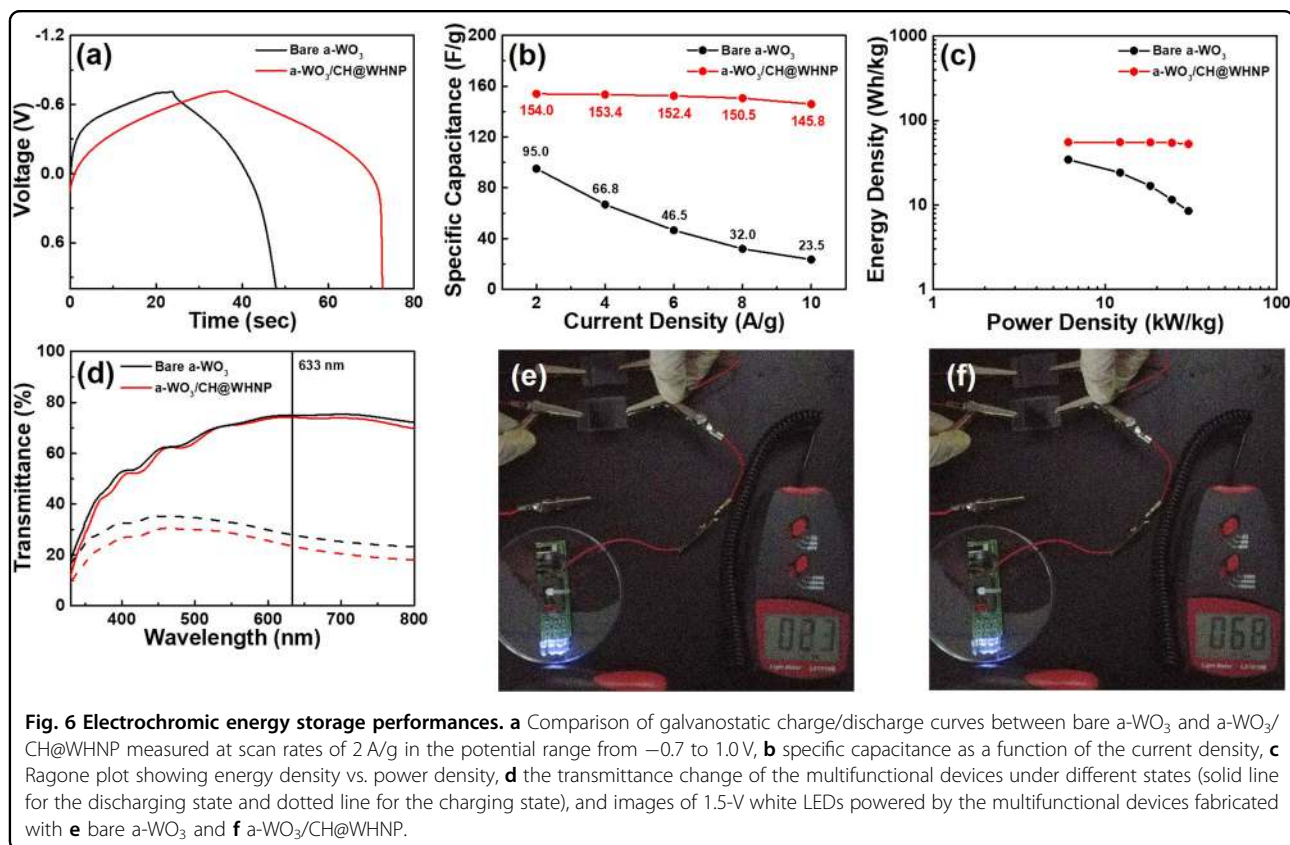


Fig. 6f) is higher than that of bare a-WO<sub>3</sub> (23.0 lux, Fig. 6e). This may be due to the enhancement of the energy density as a result of their improved electrical activity. Therefore, the use of a-WO<sub>3</sub>/CH@WHNP with advanced EC energy storage performance presents exciting possibilities for the development of multifunctional EC devices.

## Conclusions

In summary, we successfully developed novel hybrid films consisting of a WHNP-embedded chitosan thin film on a-WO<sub>3</sub> films, with enhanced EC energy storage performance. It should be emphasized that the -NH<sub>3</sub> of chitosan formed in an acidic environment that facilitated not only the formation of strong cross-linked structures to improve the electrochemical stability of the active material used in multifunctional devices, but also new chemical linking with the WHNPs. Therefore, compared to the other films, the hybrid films (a-WO<sub>3</sub>/CH@WHNP) achieved stable and fast EC performance, including fast switching speeds (4.0 s for the coloration speed and 0.8 s for the bleaching speed). This was due to the improved electrical conductivity and Li-ion diffusivity of the films, the high CE (62.4 cm<sup>2</sup>/C) associated with the increased electrochemical activity to widen the transmittance modulation, and the EC cycling retention (91.5% after 1000 cycles) caused by the relaxed electrochemical

variation of the cross-linked chitosan thin films. In terms of electrochemical energy storage performance, when compared to bare a-WO<sub>3</sub> films, a-WO<sub>3</sub>/CH@WHNP exhibited a higher specific capacitance (154.0 F/g at a current density of 2 A/g) and stable rate capability, which may be attributable to the improved electrochemical activity and electrical conductivity, respectively. Hence, multifunctional devices fabricated with this film can facilitate the production of bright illumination from 1.5-V white LEDs. Therefore, these findings are promising because they suggest that unique chemical responses can occur when an inorganic-organic hybrid is used to improve EC energy storage, thereby presenting new opportunities for practical application of WO<sub>3</sub>-based materials as fast and stable multifunctional devices.

## Acknowledgements

This work was supported by the National Research Foundation of Korea (NRF) grant funded by the Korea government (MSIT; no. 2019R1A2C1005836).

## Conflict of interest

The authors declare that they have no conflict of interest.

## Publisher's note

Springer Nature remains neutral with regard to jurisdictional claims in published maps and institutional affiliations.

**Supplementary information** is available for this paper at <https://doi.org/10.1038/s41427-019-0193-z>.

Received: 17 September 2019 Revised: 8 November 2019 Accepted: 13 November 2019.

Published online: 24 January 2020

## References

- Grätzel, M. Ultrafast colour displays. *Nature* **409**, 575–576 (2001).
- Salles, P. et al. Electrochromic effect in titanium carbide MXene thin films produced by dip-coating. *Adv. Funct. Mater.* **29**, 1809223 (2019).
- Yan, C. et al. Stretchable and wearable electrochromic devices. *ACS Nano* **8**, 316–322 (2014).
- Zhang, Q., Tsai, C.-Y., Li, L.-J. & Liaw, D.-J. Colorless-to-colorful switching electrochromic polyimides with very high contrast ratio. *Nat. Commun.* **10**, 1–8 (2019).
- Yun, T. et al. All-transparent stretchable electrochromic supercapacitor wearable patch device. *ACS Nano* **13**, 3141–3150 (2019).
- Bae, J.-W., Koo, B.-R. & Ahn, H.-J. Fe doping effect of vanadium oxide films for enhanced switching electrochromic performances. *Ceram. Int.* **45**, 7137–7142 (2019).
- Jeong, K. R. et al. Enhanced black state induced by spatial silver nanoparticles in an electrochromic device. *NPG Asia Mater.* **9**, e362 (2017).
- Koo, B.-R., Kim, K.-H. & Ahn, H.-J. Novel tunneled phosphorous-doped WO<sub>3</sub> films achieved using ignited red phosphorous for stable and fast switching electrochromic performances. *Nanoscale* **11**, 3318 (2019).
- Liu, H. S. et al. Highly transparent to truly black electrochromic devices based on an ambipolar system of polyamides and viologen. *NPG Asia Mater.* **9**, e388 (2017).
- Wu, J.-J., Hsieh, M.-D., Liao, W.-P., Wu, W.-T. & Chen, J.-S. Fast-switching photovoltachromic cells with tunable transmittance. *ACS Nano* **3**, 2297–2303 (2009).
- Besnardiere, J. et al. Structure and electrochromism of two-dimensional octahedral molecular sieve h<sup>+</sup>-WO<sub>3</sub>. *Nat. Commun.* **10**, 327 (2019).
- Li, Y., McMaster, W. A., Wei, H., Chen, D. & Caruso, R. A. Enhanced electrochromic properties of WO<sub>3</sub> nanotree-like structures synthesized via a two-step solvothermal process showing promise for electrochromic window application. *ACS Appl. Nano Mater.* **1**, 2552–2558 (2018).
- Koo, B.-R., Kim, K.-H. & Ahn, H.-J. Switching electrochromic performances improvement enabled by highly developed mesopores and oxygen vacancy defects of Fe-doped WO<sub>3</sub> films. *Appl. Surf. Sci.* **453**, 238–244 (2018).
- Cong, S., Tian, Y., Li, Q., Zhao, Z. & Geng, F. Single-crystalline tungsten oxide quantum dots for fast pseudocapacitor and electrochromic applications. *Adv. Mater.* **26**, 4260–4267 (2014).
- Lee, S.-H. et al. Crystalline WO<sub>3</sub> nanoparticles for highly improved electrochromic applications. *Adv. Mater.* **18**, 763–766 (2006).
- Baek, S.-H., Choi, K.-S., Jaramillo, T. F., Stucky, G. D. & McFarland, E. W. Enhancement of photocatalytic and electrochromic properties of electrochemically fabricated mesoporous WO<sub>3</sub> thin films. *Adv. Mater.* **15**, 15 (2003).
- Zhu, J. et al. Enhanced electrical switching and electrochromic properties of poly(p-phenylenebenzobisthiazole) thin films embedded with nano-WO<sub>3</sub>. *Adv. Funct. Mater.* **20**, 3076–3084 (2010).
- Kim, H. et al. Effect of particle size and amorphous phase on the electrochromic properties of kinetically deposited WO<sub>3</sub> films. *Sol. Energy Mater. Sol. Cells* **177**, 44–50 (2018).
- Zhang, J. et al. Multicolor electrochromic polyaniline-WO<sub>3</sub> hybrid thin films: one-pot molecular assembling synthesis. *J. Mater. Chem.* **21**, 17316 (2011).
- Gaikwad, D. K., Mali, S. S., Hong, C. K. & Kadam, A. V. Influence of disordered morphology on electrochromic stability of WO<sub>3</sub>/PPy. *J. Alloy. Compd.* **669**, 240–245 (2016).
- Ling, H., Liu, L., Lee, P. S., Mandler, D. & Lu, X. Layer-by-layer assembly of PEDOT: PSS and WO<sub>3</sub> nanoparticles: enhanced electrochromic coloration efficiency and mechanism studies by scanning electrochemical microscopy. *Electrochim. Acta* **174**, 57–65 (2015).
- Zhang, J. et al. Ultra-thin WO<sub>3</sub> nanorod embedded polyaniline composite thin film: synthesis and electrochromic characteristics. *Sol. Energy Mater. Sol. Cells* **114**, 31–37 (2013).
- Hsieh, F.-Y., Tao, L., Wei, Y. & Hsu, S.-H. A novel biodegradable self-healing hydrogel to induce blood capillary formation. *NPG Asia Mater.* **9**, e363 (2017).
- Shao, Y. et al. Investigation of nitrogen doped and carbon species decorated TiO<sub>2</sub> with enhanced visible light photocatalytic activity by using chitosan. *Appl. Catal. B* **179**, 344–351 (2015).
- Zhang, W., Li, G., Fang, Y. & Wang, X. Maleic anhydride surface-modification of crosslinked chitosan membrane and its pervaporation performance. *J. Memb. Sci.* **295**, 130–138 (2007).
- Smitha, B., Sridhar, S. & Khan, A. A. Polyelectrolyte complexes of chitosan and poly(acrylic acid) as proton exchange membranes for fuel cells. *Macromolecules* **37**, 2233–2239 (2004).
- Shigematsu, A., Yamada, T. & Kitagawa, H. Wide control of proton conductivity in porous coordination polymers. *J. Am. Chem. Soc.* **133**, 2034–2036 (2011).
- Xie, S. et al. Chitosan waste-derived Co and N Co-doped carbon electrocatalyst for efficient oxygen reduction reaction. *ChemElectroChem* **2**, 1806–1812 (2015).
- Aziz, S. B., Abdullah, O. G., Saber, D. R., Rasheed, M. A. & Ahmed, H. M. Investigation of metallic silver nanoparticles through UV-vis and optical micrograph techniques. *Int. J. Electrochem. Sci.* **12**, 363–373 (2017).
- Chen, L., Mashimo, T., Okudera, H., Iwamoto, C. & Omurzak, E. Synthesis of WO<sub>3</sub>-H<sub>2</sub>O nanoparticles by pulsed plasma in liquid. *RSC Adv.* **4**, 28673 (2014).
- Yoksan, R. & Chirachanchai, S. Silver nanoparticles dispersing in chitosan solution: preparation by  $\gamma$ -ray irradiation and their antimicrobial activities. *Mater. Chem. Phys.* **115**, 296–302 (2006).
- Koo, B.-R. & Ahn, H.-J. Fast-switching electrochromic properties of mesoporous WO<sub>3</sub> films with oxygen vacancy defects. *Nanoscale* **9**, 17788 (2017).
- Rougier, A., Rauh, D. & Nazri, G. *Electrochromic Materials and Applications: Proceedings of the International Symposium* (Electrochemical Society, Pennington, NJ, 2013).
- Pickenhahn, V. D. et al. Regioselective thioacetylation of chitosan end-groups for nanoparticle gene delivery systems. *Chem. Sci.* **6**, 4650 (2015).
- Dekamin, M. G., Azimoshan, M. & Ramezani, L. Chitosan: a highly efficient renewable and recoverable bio-polymer catalyst for the expeditious synthesis of  $\alpha$ -amino nitriles and imines under mild conditions. *Green. Chem.* **15**, 811 (2013).
- Buraidah, M. H. & Arof, A. K. Characterization of chitosan/PVA blended electrolyte doped with NH<sub>4</sub>. *J. Non-Cryst. Solids* **357**, 3261–3266 (2011).
- Chávez, E. L. et al. Theoretical studies of ionic conductivity of crosslinked chitosan membranes. *Int. J. Hyd. Energy* **35**, 12141–12146 (2010).
- Wang, X., Bai, H., Yao, Z., Liu, A. & Shi, G. Electrically conductive and mechanically strong biomimetic chitosan/reduced graphene oxide composite films. *J. Mater. Chem.* **20**, 9032–9036 (2010).
- Soltani, T., Tayyebi, A., Hong, H., Mirfasihi, M. H. & Lee, B.-K. A novel growth control of nanoplates WO<sub>3</sub> photoanodes with dual oxygen and tungsten vacancies for efficient photoelectrochemical water splitting performance. *Sol. Energy Mater. Sol. Cells* **191**, 39–49 (2019).
- Kalanur, S. S., Yoo, I.-H., Cho, I.-S. & Seo, H. Effect of oxygen vacancies on the band edge properties of WO<sub>3</sub> producing enhanced photocurrents. *Electrochim. Acta* **296**, 517–527 (2019).
- Chatten, R., Chadwick, A. V., Rougier, A. & Lindan, P. J. D. The oxygen vacancy in crystal phases of WO<sub>3</sub>. *J. Phys. Chem. B* **109**, 3146–3156 (2005).
- Vemuri, R. S., Bharathi, K., Gullapalli, S. K. & Ramana, C. V. Effect of structure and size on the electrical properties of nanocrystalline WO<sub>3</sub> films. *ACS Appl. Mater. Interfaces* **2**, 2623–2628 (2010).
- Shao, G.-S., Wang, F.-Y., Ren, T.-Z., Liu, Y. & Yuan, Z.-Y. Hierarchical mesoporous phosphorous and nitrogen doped titania materials: synthesis, characterization and visible-light photocatalytic activity. *Appl. Catal. B-Environ.* **92**, 61–67 (2009).
- Bulusheva, L. G. et al. Electrochemical properties of nitrogen-doped carbon nanotube anode batteries. *Carbon* **49**, 4013–4023 (2011).
- Kang, Y.-G., Vu, H. C., Le, T. T. & Chang, Y.-S. Activation of persulfate by a novel Fe(II)-immobilized chitosan/alginate composite for bisphenol A degradation. *Chem. Eng. J.* **353**, 736–745 (2018).
- Wang, Y., Li, B. & Zhou, Y. In situ mineralization of magnetite nanoparticles in chitosan hydrogel. *Nanoscale Res. Lett.* **4**, 1041–1046 (2009).
- Koo, B.-R., Oh, D.-H., Riu, D.-H. & Ahn, H.-J. Improvement of transparent conducting performance on oxygen-activated fluorine-doped tin oxide electrodes formed by horizontal ultrasonic spray pyrolysis deposition. *ACS Appl. Mater. Interfaces* **9**, 44584–44592 (2017).
- Koo, B.-R., Oh, D.-H. & Ahn, H.-J. Influence of Nb-doped TiO<sub>2</sub> blocking layers as a cascading band structure for enhanced photovoltaic properties. *Appl. Surf. Sci.* **433**, 27–34 (2018).



49. Wang, K., Wu, H., Meng, Y., Zhang, Y. & Wei, Z. Integrated energy storage and electrochromic function in one flexible device: an energy storage smart window. *Energy Environ. Sci.* **5**, 8384 (2012).
50. Koo, B.-R., Bae, J.-W. & Ahn, H.-J. Optoelectronic multifunctionality of combustion-activated fluorine-doped tin oxide films with high optical transparency. *Ceram. Int.* **45**, 10260–10268 (2019).
51. Gan, J. K., Lim, Y. S., Huang, N. M. & Lim, H. N. Boosting the supercapacitive properties of polypyrrole with chitosan and hybrid silver nanoparticles/nanoclusters. *RSC Adv.* **6**, 88925 (2016).
52. Bian, J. et al. Preparation and characterization of modified graphite oxide/poly(propylene carbonate) composites by solution intercalation. *Polym. Degrad. Stabil.* **96**, 1833–1840 (2011).
53. Pernites, R. B., Ponnampati, R. R. & Advincula, R. C. Superhydrophobic–superoleophilic polythiophene films with tunable wetting and electrochromism. *Adv. Mat.* **23**, 3207–3213 (2011).
54. Chang, J. et al. Activated porous carbon prepared from paulownia flower for high performance supercapacitor electrodes. *Electrochim. Acta* **157**, 290–298 (2015).
55. Wei, X. & Shen, P. K. Electrochromics of single crystalline WO<sub>3</sub>·H<sub>2</sub>O nanorods. *Electrochem. Commun.* **8**, 293–298 (2006).
56. Ding, J.-R. & Kim, K.-S. 1-D WO<sub>3</sub>@BiVO<sub>4</sub> heterojunctions with highly enhanced photoelectrochemical performances. *Chem. Eng. J.* **334**, 1650–1656 (2018).
57. Li, S., Chen, J., Gong, X., Wang, J. & Lee, P. S. Holey graphene-wrapped porous TiNb<sub>2</sub>O<sub>6</sub> microparticles as high performance intercalation pseudocapacitive anode materials for lithium-ion capacitors. *NPG Asia Mater.* **10**, 406–416 (2018).
58. An, G.-H., Koo, B.-R. & Ahn, H.-J. Activated mesoporous carbon nanofibers fabricated using water etching-assisted templating for high-performance electrochemical capacitors. *Phys. Chem. Chem. Phys.* **18**, 6587–6594 (2016).
59. Kim, K.-H., Koo, B.-R. & Ahn, H.-J. Sheet resistance dependence of fluorine-doped tin oxide films for high-performance electrochromic devices. *Ceram. Int.* **44**, 9408–9413 (2018).
60. Li, H., McRae, L., Firby, C. J. & Elezabi, A. Y. Rechargeable aqueous electrochromic batteries utilizing Ti-substituted tungsten molybdenum oxide based Zn<sup>2+</sup> ion intercalation cathodes. *Adv. Mater.* **31**, 1807065 (2019).
61. Xie, S. et al. Electrodeposited Mo-doped WO<sub>3</sub> films with large optical modulation and high areal capacitance toward electrochromic energy-storage applications. *Appl. Surf. Sci.* **459**, 774–781 (2018).